OPTICAL PERFORMANCES OF LENSLESS SUB-2MICRON PIXEL FOR APPLICATION IN IMAGE SENSORS

R. Marinelli[*] and E. Palange

Dipartimento di Ingegneria Elettrica e dell'Informazione, Università dell'Aquila, Via G. Gronchi 18, 67100 L'Aquila, Italy

Abstract—In this paper we will report on the optical performances of submicron planar lensless pixels arranged in the 2×2 Bayer cell configuration, the basic element of CMOS colour image sensors. The 2D microlens array placed in front of each pixel in commercial devices has been replaced by a 2D array of submicron holes realised on a thin metal film. Each pixel has been designed to present a lightpipe inside its structure acting as an optical waveguide that confines the light up to photodiode surface. This pixel design is fully compatible with large scale industry production since its fabrication involves only standard lithographic and etching procedures. Simulations of the light propagation inside the lensless pixel has been performed by using full 3D electromagnetic analysis. In this way it was possible to determine the optical performances of the Bayer cell in terms of the normalized optical efficiency and crosstalk effects between adjacent pixels that result to be up to 30% and a factor 10, respectively, better than those ones obtained for the microlens counterpart. The significant increase of the achievable values of the normalized optical efficiency and crosstalk can foresee the possibility to reduce the pixel size down to 1 µm, i.e., beyond the limit imposed by the diffraction effects arising in microlens equipped pixel.

1. INTRODUCTION

The investigation of simple methods based on nanosized structures to achieve nanofocusing of light in the visible region is currently an interesting topic of research for those optical applications like digital imaging and confocal microscopy in which a further increase of the spatial resolution and/or the photosensitive area is a challenging task.

Complementary metal oxide semiconductor (CMOS) image sensors are typical examples of devices for which the increase of the spatial resolution implies the reduction of their pixel dimensions that are, presently, reaching a size only few times larger than the wavelength of the light in the visible region of the electromagnetic spectrum. At present, the downscaling process limits the smallest achievable pixel size in the 1.75 to 1.4 μm range for large device production. The state of the art of the CMOS-based image sensor technology employs a refractive microlens located at the pixel entrance to focus the light on the photodiode surface. Downscaling of the pixel size requires to improve the optical and physical properties of the materials used to fabricate the microlenses with progressively smaller diameters and larger numerical apertures. This is mainly related to the fact that the technological processes employed in the large scale device production do not allow, at present, a further reduction of both the thickness of the optical stack hosting the metal lines used for the electrical connections and the distance between adjacent pixels. On the other hand, from the point of view of the physical mechanisms, it has been recently demonstrated that for pixel size smaller than 1.4 μm, diffraction effects become so significant to limit the effectiveness of the microlens focusing properties [1] and this, in turn, produces large optical crosstalk effects between adjacent pixels that are significant also for pixel size close to 3.9 μm [2]. Advances in material research make now possible to exploit the possibility to replace front-side illuminated image sensors with the back-side illuminated counterparts in order to reduce the pixel thickness at least for what concerns the optical path and increase the optical efficiency and the device fill factor [3, 4]. Even in this case the research of novel focusing components and/or pixel structures is mandatory to fully exploit the potentiality of this new paradigm. Different designs of planar lenses and reflectors based on submicron and nanometer slits periodically [5] and non-periodically [6, 7] distributed on metal films have been reported. In these optical components the required lens phase profile is provided by a properly choice of the number and width of the slits as far as of their mutual distance. The extraordinary optical transmission of the planar lenses is accomplished by the generation and propagation of surface plasmon-polariton modes confined at the slit metal surface without suffering radiation away. By using these lenses it has been demonstrated that it is possible to obtain 0.88 μm width spot size at full-width at half-maximum and focal length of 5 μm [6]. More recently, it has been proposed a more complex structure (the metalens) that combines a planar lens with a metamaterial slab. By numerical analysis, it was demonstrated that this structure is able to provide

phase compensation and wave matching mechanism allowing to obtain super resolution focusing [8]. Even though the planar lenses are interesting structures because they permit to realize optical devices using the same technology employed in the CMOS image sensor manufacturing, the fabrication of the slits, the core elements of the lens, implies the use of lithographic and etching procedures at the nanometer scale that are still far from being introduced in the large scale opto-electronic industry. At the laboratory level, in fact, such structures can be fabricated using electron beam nano-lithography while chemical and/or etching processes need to be carefully tested to obtain reliable devices. In CMOS-based image sensor technology one adopted solution that allows for a more effective light focalization on the photodiode and a decrease of the optical cross-talking effects, is the use of the guiding properties of a lightpipe created between the microlens and the photodiode surface [9, 10]. The lightpipe is realized by making use of a polymer with a refractive index higher than those ones of the surrounding oxides layers that form the pixel. As a consequence, light entering the lightpipe through the microlens experiences optical confinement up to the photodiode and, at the same time, the frustrated total internal reflection mechanism generates evanescent waves that can couple into the adjacent lightpipes exchanging energy between neighbouring pixels and giving rise to optical crosstalk effects. In the present paper we will make use of this pixel structure replacing the microlens with a simple sub-micron aperture produced on a thin metal film. We will prove that light diffracted from the aperture, mediated by the generation of surface plasmon-polariton modes, is entirely confined within the lightpipe. Under suitable conditions, this produces a beaming of the light inside the pixel toward the photodiode area. Thus, the proposed pixel structure uses the diffraction effects that are, however, detrimental for microlens equipped pixel. Full three dimensional (3D) simulations operated on a Bayer cell composed of four pixels demonstrate that it is possible to obtain optical efficiencies and crosstalk rejection between adjacent pixels 30% and a factor 12 respectively better than those ones obtained in similar pixels equipped with microlenses for pixel sizes close to $0.97\,\mu m$. For pixels equipped with microlens, this size has been demonstrated to be the limiting pixel size below which the optical performances are strongly degraded by diffraction [1].

2. THREE DIMENSIONAL PIXEL MODEL

Full 3D simulations of the light propagation inside the image sensor pixel have been based on the finite integration technique [11–13]

in which the physical space is divided in cubic grids forming a hexahedral mesh. The size of the cubic grid was set equal to $\lambda/10$ where λ is referred to the shortest wavelength of the electromagnetic spectrum used in the simulations. Moreover, the software used for the simulations (CST Microwave Studio 2010) provides an adaptive meshing tool to fix the integration step respect to the size of the structure to be simulated and the values and frequency dispersion curves of the permittivity of the different materials utilized for the pixel fabrication. The physical model employs a basic structure of four pixels forming a 2×2 structure in the configuration of a single Bayer cell in which two diagonal pixels are used to reveal the green component of the incident light while the other two are for the red and blue components. The cross section of a single pixel is shown in Fig. 1(a). The basic structure of the pixel is the Inter Layer Dielectric (ILD) composed of several silicon oxide layers grown on top of the Si photodiode surface. In real image sensors, ILD holds the metal lines for the electrical connections. Along the direction perpendicular to each Si photodiode surface, a conical hole is produced in the ILD by chemical etching. The hole is thus filled with a polymer having a refractive index higher than those ones of the surrounding ILD silicon oxides and this produces an optical waveguide (the lightpipe) for the

(a)   (b)   (c)
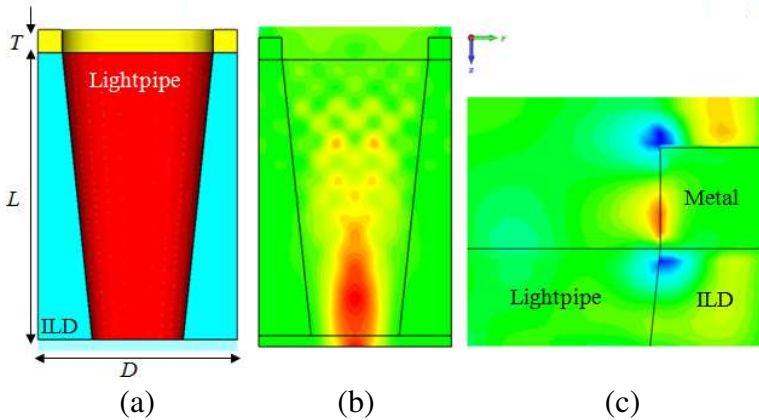
Figure 1. (colour online): panel (a) the cross-section model of each single pixel of the Bayer cell used for simulations: T is the Au film thickness, L the length of the ILD and of the lightpipe, and D is the pixel size; panel (b) the 2D plot of the z-component of the Poynting vector at $\lambda_g = 550\,\text{nm}$; panel (c) the surface plasmon-polaritons (E_z field) confined at the metal-air interface of the aperture.

light impinging at the pixel surface through the mechanism of the total internal reflection. In our simulations the radius of the circular section at the bottom of the lightpipe, i.e., the photodiode area, was fixed equal to $0.4\,\mu m$, the pixel size, D, was varied from 1.75 to $0.97\,\mu m$ and the ILD thickness, L, was set equal to $2.5\,\mu m$. For each pixel size, the radius of the lightpipe section at the pixel entrance depends on the value of the lightpipe tapering angle ϑ (in our case ranging from $0°$ to $6°$) that is choesen to optimize the light confinement and/or preserve the pixel aspect ratio. On top of the ILD is deposited a metal thin film (thickness $T = 0.2\,\mu m$) on which circular apertures are produced in correspondence of each lightpipe entrance. In image sensor manufacturing procedure, these apertures can be obtained by using conventional lithographic and etching processes. For simulations gold was chosen to reduce the computational times respect to aluminum, the more commonly employed metal in electronic industry.

For simulation purposes, we placed open boundary conditions (i.e., perfectly matched layer) at the Bayer cell top and bottom surfaces perpendicular to the light propagation direction and 2-dimensional (2D) periodic boundary conditions at the lateral sides of the Bayer cell. Instead to use at the pixel bottom a Si substrate with an antireflection coating on its surface, we preferred to introduce an index matching layer between the ILD and the perfect matched layer. Apart from the selected choice of the bottom final layer or substrate, we note that this procedure must be always used to prevent numerical instabilities and result inaccuracies. We simplified the Bayer cell model omitting the insertion of the color filters on top of the apertures because their permittivity frequency dispersive relations generally depend on the specific micro-fabrication techniques. However, this does not represent a limitation in describing the overall optical behavior of the Bayer cell at different wavelengths because, by using the time solver tool, CST Microwave Studio allows in a single simulation to analyze the 3D e.m. field distribution inside each pixel in the frequency spectrum corresponding to wavelengths ranging from 450 to 633 nm. Once the simulation is terminated, it is possible to insert 3D monitors located at the photodiode surfaces and centered at some selected wavelengths that return the Poynting vector plots by computing the inverse Fourier transform of the e.m. field distribution. In particular, we have selected the following three wavelengths $\lambda_b = 450\,nm$, $\lambda_g = 550\,nm$ and $\lambda_r = 633\,nm$ as the central wavelengths for the blue, green and red spectral bands of visible light, respectively.

In performing the numerical simulations we used a continuous plane wave with an amplitude of 1V/m impinging from air at normal incidence on the pixel surface. The permittivity frequency dispersion

curves of the silicon oxide and of the polymer have been obtained from
Refs. [14] and [9], respectively. For gold, instead, we used the Drude-
critical points model as discussed in Ref. [15].

In Fig. 1(b) we show the 2D Poynting vector plot describing
the energy flow inside the lightpipe from the aperture toward the
photodiode for green light centered at $\lambda_g = 550 \, \text{nm}$. For this
wavelength the transmitted light is confined inside the lightpipe and
the spotsize is smaller than the photodiode area. Similar results
are obtained for the other two selected wavelengths, λ_b and λ_r. In
particular, we verified that the focalization is more effective for light of
smaller wavelengths even though an efficient energy transfer is always
obtained for the three wavelengths as will be discussed later on. The
guiding properties of the lensless pixel is guaranteed by combining the
diffraction effects arising from the presence of the apertures on the gold
film and the guiding properties of the lightpipe by means of the total
internal reflection effect. Since the diameter of the aperture is close to
the input wavelength, the light emerging from the aperture is diffracted
at angles much higher than the internal total reflection angle occurring
in the lightpipe thus guaranteeing light confinement. Furthermore,
light transferred through the apertures is assisted by the generation
of surface plasmon-polariton modes that are generated at the metal
surface of the aperture along the beam propagation direction. This
mechanism has been used to explain the increase of light transmission
through nanometer size apertures [16, 17] but, as reported in Fig. 1(c),
is also effective for larger apertures like those ones here discussed. In
Fig. 1(c) it is shown the y-z section of the right lateral side of the pixel:
at the aperture edge, the electric field associated to the input e.m.
plane wave suffers large diffraction effects and the components having
wavevectors matching the surface plasmon-polariton modes propagate
through the aperture reaching the lightpipe. At the aperture edge,
diffraction from the metal surface shifts the phase of the electric field
whose amplitude has the maximum along a direction opposite to the y-
axis. In Fig. 1(c) is reported the electric field associated to the surface
plasmon-polariton mode taken at an arbitrary value of the incident
e.m. field phase. In this case the input light is transverse magnetic
(TM) polarized. We verified that a transverse electric (TE) polarized
light does not produce, as expected, any surface plasmon-polariton
excitation. On the other hand, if the input light is TE polarized, the
surface plasmon-polariton modes arise at the aperture lateral sides that
are $90°$ degrees rotated respect to those ones of Fig. 1(c) on the x-z
plane.

3. RESULTS OF THE SIMULATIONS

The optical performances of the modeled pixel have been studied by analyzing the results of the simulations in terms of Normalized Optical Efficiency (NOE) and Normalized Optical Crosstalk (NOX) [1]. The first of these two parameters derives from the optical efficiency, also named external quantum efficiency, that represents the fraction of the optical power impinging on the photodiode area respect to that one incident on the pixel surface [18]. The second parameter is related to the optical crosstalk that measures the fraction of the average optical power that reaches the photodiode area of the adjacent pixels respect to that one incident on the surface of any selected pixel [19]. Based on these definitions, NOE is defined as the ratio between the optical power delivered at the photodiode area, in our case the bottom lightpipe area, and the total power measured in the domain of the four pixels forming the Bayer cell. In particular, the simulations have been performed illuminating only one pixel by masking the others three using perfect absorber filters. On the other hand, NOX is defined as the ratio between the averaged optical power delivered at the photodiode areas of the three adjacent masked pixels and the total received optical power. The corresponding mathematical expressions of NOE and NOX are:

$$
\eta_{\mathrm{NOE}}(\lambda) = \frac{\iint\limits_{LP\,area} S_z(\lambda)dxdy}{\iint\limits_{domain} S_z(\lambda)dxdy}
$$

$$
\eta_{\mathrm{NOX}}(\lambda) = \frac{\frac{1}{3}\sum\limits_{i=1}^{3}\iint\limits_{adjacent\,pixels,i} S_z(\lambda)dxdy}{\iint\limits_{domain} S_z(\lambda)dxdy}, \tag{1}
$$

where S_z is the z-component of the Pointing vector along the beam propagation direction. The integral domains *LP area*, *adjacent pixels* and *domain* indicate the lightpipe bottom area, the bottom area of each pixel adjacent to that one illuminated and the area of the entire Bayer cell at the photodiode surface, respectively. Respect to 2D simulations in which a linear array of five pixels constitutes the computational basic structure for the calculation system [1], the 3D simulations performed in this paper use as computational basic structure the Bayer cell before described for which two of the adjacent pixels located along one of the cell diagonal both detect green light. This fact relaxes the crosstalk requirements for these pixels. However, in calculating the NOX parameter we did not take this fact into consideration since NOX is the signature of the light transferred inside each pixel and this
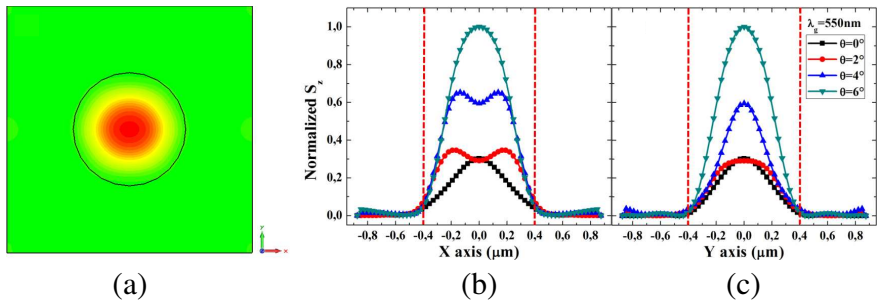
Figure 2. (colour online): characteristics of the transmitted beam at the photodiode surface for a TM polarized input light at $\lambda_g = 550$ nm, for different values of the tapering angle ϑ. Panel (a) beam spot size; panel (b) beam profiles along the x-axis; panel (c) beam profiles along the y-axis. For a TE polarized input light the plot of panel (b) and (c) are inverted. Vertical dotted lines indicate the photodiode surface side. The photodiode surface center is located at $x = y = 0$.

is independent from the fact that two pixels detect light at the same wavelength.

In Fig. 2(a) we report the typical spot-size at the photodiode surface. The spot-size is not perfectly circular as results also from the different profiles along the x- and y-axis shown in Figs. 2(b) and (c), respectively. These figures report the beam profiles measured at the photodiode input surface obtained with the lightpipe tapering angle ϑ varying from 0° to 6° for a pixel size of 1.75 μm and an input TM polarized light. The beam profile along the x-axis changes from a bell-shaped profile ($\vartheta = 0°$) to a double peak profile for ϑ ranging from 2° to 4° and resulting again a bell-shaped profile for $\vartheta = 6°$. On the other hand, the corresponding beam profiles along the y-axis measured under the same conditions always show bell-shaped profiles. The different behaviors of the beam profiles along the two orthogonal x- and y-axes are related to the presence of plasmon-polariton modes, as before discussed. In this case, for TM polarized light, the plasmon-polariton modes lays on the y-z plane. On the other hand, if a TE polarized input light is considered, we verified that the beam profiles of Figs. 2(b) and (c) are reversed since now the surface plasmon-polariton modes occur at the internal surface of the aperture 90° rotated respect to the case of Figs. 2(b) and (c).

In Fig. 3 we report the normalized intensity beam profiles at the photodiode surface along the x- and y-axis as measured between two adjacent pixels along one side of the Bayer cell for an input TM
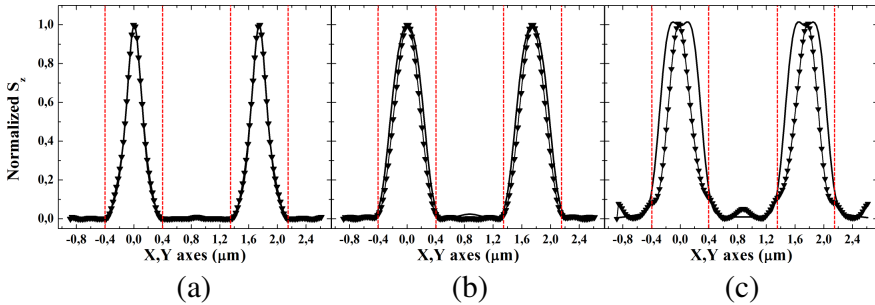
Figure 3. Normalized intensity beam profiles at the photodiode surface for two adjacent pixels of the Bayer cell taken along the x-axis (solid line) and y-axis (triangles) for a TM polarized input light. Pixel size and lightpipe tapering angle are $1.75\,\mu$m and $6°$, respectively. Panel (a) blue component centered at $\lambda_b = 450$ nm; (b) green component centered at $\lambda_g = 550$ nm; (c) red component centered at $\lambda_r = 633$ nm. Vertical dotted lines indicate the photodiode surface side.

polarized light and a lightpipe tapering angle equal to $\vartheta = 6°$. The beam profiles of Figs. 3(a), (b) and (c) are referred to the three selected wavelengths λ_b, λ_g and λ_r respectively. We note that light confinement becomes less effective at the greater wavelengths and this is due to the fact that for apertures with the same size, when the wavelength increases diffraction effects become more effective and the value of the polymer refractive index decreases. The confinement effect could be optimized by choosing for each selected wavelength the aperture size that optimizes the light propagation inside the lightpipe and/or by using high refractive index polymers. Aperture optimization can be achieved by adapting the lithographic mask to produce the desired 2D-array pattern on the metal film. A more refined optimization process involving the variation of the tapering angles for each selected wavelength is unrealistic since it cannot be easily implemented at the level of large scale production.

In order to determine the NOE and NOX we performed simulations similar to those ones reported in Fig. 3 for a pixel size ranging from 0.97 to $1.75\,\mu$m. In particular, for each pixel size, the aperture and the corresponding lightpipe tapering angle were chosen to obtain the best possible performances for the three selected wavelengths λ_b, λ_g and λ_r. The results of the calculations (triangles) are plotted in Fig. 4 together with the data (circles) of similar simulations taken from Ref. [1] in which the authors discussed the
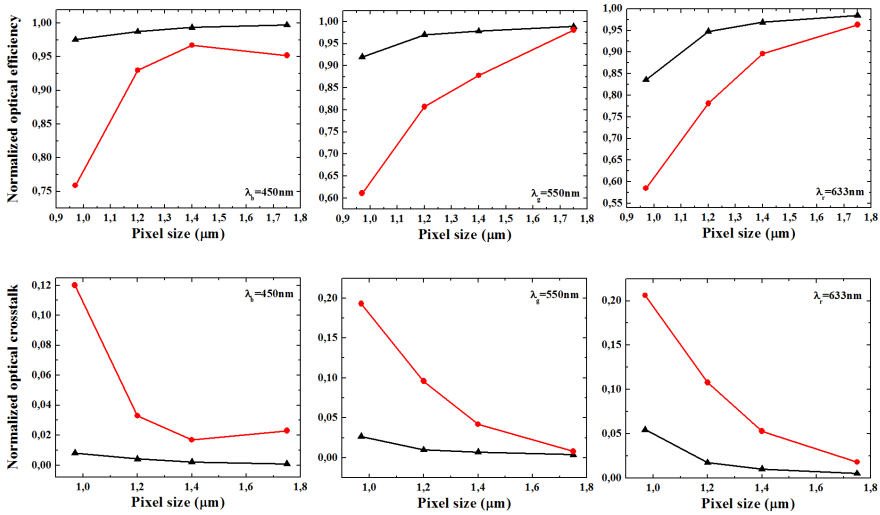
Figure 4. (colour online): (top panel) the normalized optical efficiency and, (bottom panel), the normalized optical crosstalk as a function of the pixel size for the three selected wavelengths. Triangles and circle refer to the data of the present paper and those ones of Ref. [1], respectively.

limits in downscaling the pixel size due to diffraction effects originated by the presence of the microlense located at the pixel entrance. In particular, as shown in Fig. 4 (top panel), for both lensless and microlens equipped pixels, NOE decreases as the pixel size decreases. However, the replacement of the microlens with a simple aperture at the pixel entrance gives better results independently from the pixel size. This finding is particularly significant for the smaller values of the pixel size. Considering, in fact, a pixel size $D = 0.97\,\mu$m, respect to the microlens geometry, the lensless pixel counterpart improves the normalized optical efficiency of about 30%, 33% and 22% for the blue, green and red wavelengths, respectively. It is important to underline that for the lensless geometry, diffraction effects are not detrimental for the pixel overall optical performances since, in this case, the diffracted light is strongly coupled to the lightpipe. The final result is that in the range of the pixel size of Fig. 4 (top panel), NOE never decreases below 0.80 for red light and remains above 0.90 for the green and blue light. These findings are confirmed by analyzing the NOX results plotted in Fig. 4 (bottom panel). Also for this parameter the obtained values for the blue, green and red wavelengths are better than the corresponding values reported in Ref. [1] by a factor 12, 8, 4, respectively. In
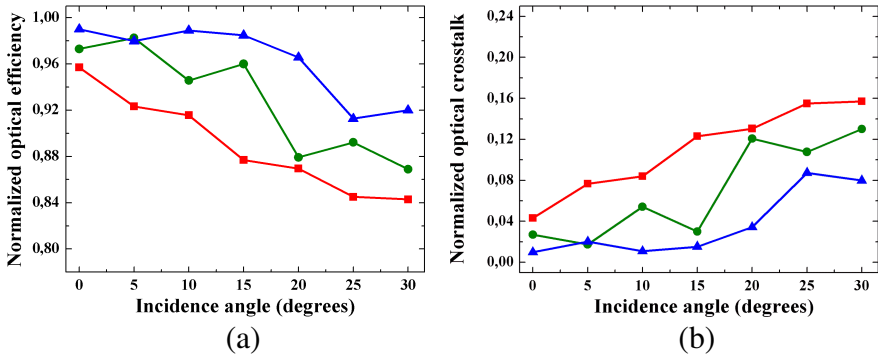
Figure 5. (a) Dependence of the normalized optical efficiency and (b) normalized optical crosstalk as a function of the incident angle of a TM-polarised input beam. Pixel size is $1.75\,\mu$m. Triangles, dots and squares refer to the data obtained for $\lambda_b = 450\,$nm, $\lambda_g = 550\,$nm and $\lambda_r r = 633\,$nm reference wavelengths, respectively.

microlens equipped pixels, the microlens are designed to achieve strong focalization at the photodiode plane for incident angles of the e.m wave different from zero. To complete the study of the beaming properties of the lensless pixel configuration, we performed 2D numerical simulations to evaluate NOE and NOX parameters as a function of the incidence angle for a TM polarized e.m. wave and a pixel size equal to $1.75\,\mu$m. The results are reported in Fig. 5.

The incident angle was varied in the range from 0 to 30 degrees. For larger values of the incident angle the sensitivity of the image sensor with microlens equipped pixels has been reported to sharply drop also for pixel size of $2.2\,\mu$m and it is only partially compensated by replacing refractive microlenses with more complex digital microlenses [20]. From the results of Fig. 5(a), NOE decreases for a value of 7.6%, 12.0% and 14% for the blue, green and red selected wavelengths, respectively, within the entire range of variation of the incident angle. Corresponding enhancements in percentage of the NOX values have been obtained at the three reference wavelengths as shown in Fig. 5(b). The results of Fig. 5 demonstrate that the beaming properties of the lensless pixel structure continues to be very efficient also for incident angles different from the normal incidence.

Finally, in order to compare the results obtained with the lensless pixel geometry with those ones of [10] in which the authors used pixels equipped with microlens on top of the lightpipe, we performed 2D simulations on the Bayer cell to obtain the optical efficiency and crosstalk. By taking the same conditions of Ref. [10] for the

polymer refractive index ($n = 1.6$) used to implement the lightpipe and the pixel size of $D = 1.75\,\mu\text{m}$, pixel models based on lensless and microlens geometries return the same values for the optical efficiency and crosstalk. We can conclude that also in this case, the lensless geometry simplifies the pixel fabrication avoiding the use of a microlens and does not degrade the overall optical performances.

4. CONCLUSIONS

We have demonstrated that lensless pixels arranged in the Bayer cell configuration as used in commercial image sensor devices and making use of lightpipe structure have better optical performances respect to those ones obtained for pixels equipped with microlenses located at their entrance. By performing full 3D electromagnetic simulations of the light propagation inside the Bayer cell, we have shown that in terms of the normalized optical efficiency and crosstalk, the lensless pixel geometry is always more efficient respect to the microlens equipped counterpart. In particular, simulations demonstrate that the decrease of the normalized optical efficiency and the increase of the crosstalk effects as a function of the reduction of the pixel size is largely less effective for the lensless pixel geometry and this can foresee the real possibility to decrease the pixel size for values less than $1\,\mu\text{m}$. Moreover, the proposed geometry is completely compatible with the actual large scale image sensor manufacturing process and overcomes the problems related to the fabrication of microlenses with large numerical apertures.

REFERENCES

1. Huo, Y., C. C. Fesenmaier, and P. B. Catrysse, "Microlens performance limits in sub-2 μm pixel CMOS image sensors," *Optics Express*, Vol. 18, No. 6, 5861–5872, 2010.
2. Hsu, T. H., Y. K. Fang, D. N. Yaung, S. G. Wuu, H. C. Chien, C. S. Wang, J. S. Lin, C. H. Tseng, S. F. Chen, C. S. Lin, and C. Y. Lin, "Dramatic reduction of optical crosstalk in deep-submicrometer CMOS imager with air gap guard ring," *IEEE Electron Dev. Lett.*, Vol. 25, No. 6, 375–377, 2004.
3. Swain, P. K. and D. Cheskis, "Back-illuminated image sensors come to the forefront," *Photonics Spectra*, Issue August, 2008.
4. Dragoi, V., A. Filbert, S. Zhu, and G. Mittendorfer, "CMOS wafer bonding for back-side illuminated image sensors fabrication," *11th*

International Conference on Electronic Packaging Technology & High Density Packaging, 27–30, August 2010.

5. Lezec, H. J., A. Degiron, E. Devaux, R. A. Linke, L. Martin-Moreno, F. J. Garcia-Vidal, and T. W. Ebbesen, "Beaming light from a subwavelength aperture," *Science*, Vol. 297, 820–822, 2002.

6. Verslegers, L., P. B. Catrysse, Z. Yu, J. S. White, E. S. Barnard, M. L. Brongersma, and S. Fan, "Planar lenses based on nanoscale slit arrays in a metallic film," *Nanoletters*, Vol. 9, No. 1, 235–238, 2009.

7. Shi, H., C. Wang, C. Du, X. Luo, X. Dong, and H. Gao, "Beam manipulating by metallic nano-slits with variant witdths," *Optics Express*, Vol. 13, No. 18, 6815–6820, 2005.

8. Ma, C. and Z. Liu, "A super resolution metalens with phase compensation mechanism," *Appl. Phys. Lett.*, Vol. 96, 183103, 2010.

9. Gambino, J., B. Leidy, J. Adkisson, M. Jaffe, R. J. Rassel, J. Wynne, J. Ellis-Monaghan, T. Hoague, D. Meatyard, S. Mongeon, and T. Kryzak, "CMOS Imager with copper wiring and lightpipe," *International Electron Device Meeting, IEDM'06*, Technical Digest, San Francisco, USA, December 2006.

10. Fesenmaier, C. C., Y. Huo, and P. B. Catrysse, "Optical confinement methods for continued scaling of CMOS image sensor pixels," *Optics Express*, Vol. 16, No. 25, 20457–20470, 2008.

11. Weiland, T., "A discretization method for the solution of Maxwell's equations for six component fields," *Electron. Commun.*, Vol. 31, 116, 1977.

12. Clemens, M. and T. Weiland, "Discrete electromagnetism with the finite integration technique," *Progress In Electromagnetics Research*, Vol. 32, 65–87, 2001.

13. Weiland, T., "Time domain electromagnetic field computation with finite difference methods," *Int. J. Numer. Model.*, Vol. 9, No. 4, 295–319, 1996.

14. Palik, E. D., *Handbook of Optical Constants of Solids*, Academic Press, 1998.

15. Vial, A. and T. Laroche, "Comparison of gold and silver dispersion law suitable for FDTD simulations," *Applied Physics B*, Vol. 93, No. 1, 139–143, 2008.

16. Ebbesen, T. W., H. J. Lezec, H. F. Ghaemi, T. Thio, and P. A. Wolff, "Extraordinary optical transmission through sub-wavelength hole arrays," *Nature*, Vol. 391, 667–669, February 1998.

17. Ghazi, G. and M. Shahabadi, "Modal analysis of extraordinary transmission through an array of subwavelength slits," *Progress In Electromagnetics Research*, Vol. 79, 59–74, 2008.

18. Nakamura, J., *Image Sensors and Signal Processing for Digital Still Cameras*, Chapter 5, Taylor and Francis Group, Boca Raton, USA, 2006.

19. Agranov, G., V. Berezin, and R. H. Tsai, "Crosstalk and microlens study in a color CMOS image sensor," *IEEE Trans. Electron Dev.*, Vol. 50, No. 1, 4–11, January 2003.

20. Onozawa, K., K. Toshikiyo, T. Yogo, M. Ishii, K. Yamanaka, T. Matsuno, and D. Ueda, "A MOS image sensor with a digital-microlens," *IEEE Trans. Electron Dev.*, Vol. 55, No. 4, 986–991, April 2008.